PHYSICAL REVIEW D

PARTICLES AND FIELDS

THIRD SERIES, VOLUME 25, NUMBER 11 1 JUNE 1982

Measurement of neutrino-proton and antineutrino-proton elastic scattering

J. Horstkotte,* A. Entenberg,† R. S. Galik,‡ A. K. Mann, and H. H. Williams
Department of Physics, University of Pennsylvania, Philadelphia, Pennsylvania 19104

W. Kozanecki,§ C. Rubbia, J. Strait,|| and L. Sulak¶
Department of Physics, Harvard University, Cambridge, Massachusetts 02138

P. Wanderer
Brookhaven National Laboratory, Upton, New York 11973
(Received 4 December 1981)

We report here new measurements of neutrino-proton and antineutrino-proton elastic scattering, performed in the BNL neutrino beam. We observed a net signal of 212 neutrino events and 110 antineutrino events which lead to determination of the values $R_\nu \equiv \sigma(\nu_\mu + p \to \nu_\mu + p)/\sigma(\nu_\mu + n \to \mu^- + p) = 0.11 \pm 0.015$, $R_{\bar\nu} \equiv \sigma(\bar\nu_\mu + p \to \bar\nu_\mu + p)/\sigma(\bar\nu_\mu + p \to \mu^+ + n) = 0.19 \pm 0.035$, and $R^{\rm NC} \equiv \sigma(\bar\nu_\mu + p \to \bar\nu_\mu + p)/\sigma(\nu_\mu + p \to \nu_\mu + p) = 0.41 \pm 0.09$ for $0.40 < Q^2 < 0.90$ (GeV/c)^2 where $-Q^2$ is the square of the momentum transfer to the nucleon. The differential cross sections as functions of Q^2, $d\sigma^\nu/dQ^2$ and $d\sigma^{\bar\nu}/dQ^2$, are also determined. Our results are in good agreement with the Weinberg-Salam-Glashow-Iliopoulos-Maiani model of the weak and electromagnetic interactions and yield $\sin^2\theta_W = 0.28 \pm 0.03$.

INTRODUCTION

Neutrino-proton and antineutrino-proton elastic scattering ($\nu_\mu + p \to \nu_\mu + p$ and $\bar\nu_\mu + p \to \bar\nu_\mu + p$) are particularly attractive channels with which to study the weak hadronic neutral current. This reaction is the neutral-current analog of neutron β decay, the careful measurement of which was instrumental in determining the V/A theory of charged-current interactions. Experimental results are easily interpreted. The one observable final-state particle (the proton) is well understood, and the measurement of its kinematic variables constrains the entire reaction. No model-dependent assumptions are required: no strong-interaction corrections are necessary as in single-pion production, and no "new phenomena" are involved as in deep-inelastic scattering.

The great success of the Weinberg-Salam model[1] with the Glashow-Iliopoulos-Maiani mechanism[2] (WS-GIM model) makes it very important to look at any measurements of weak-neutral-current phenomena in the light of its predictions. Our measurements of the total and differential cross sections for neutrino-proton and antineutrino-proton elastic scattering allow us to make detailed comparisons to the WS-GIM model. We can look both for consistency with the model within our measurements and for consistency with the results of other experiments as well. We are also able to extract important information about the structure of the weak neutral current in a model-independent way.

Several bubble-chamber searches for these reactions[3,4] gave null results due to low rates and high backgrounds. The neutrino channel was first observed in 1976 by the Columbia-Illinois-Rockefeller[5] (CIR) and Harvard-Pennsylvania-Wisconsin[6] (HPW) collaborations at Brookhaven National Laboratory (BNL). It was later confirmed at CERN.[7,8] Elastic antineutrino-proton scattering was observed[9] by the HPW collaboration and was later confirmed by the Columbia-Illinois-BNL (CIB) collaboration.[10]

In this report we discuss new high-statistics measurements of both neutrino-proton and antineutrino-proton elastic scattering. The measurements consist of two separate data samples which were taken at different times and analyzed separately and independently. Data set A contains data which have been reported previously.[11] Data set B contains data which have not been previously reported. We concentrated on antineutrino running in data set B, gathering an antineutrino sample more than twice the size of that in data set A, while gathering a neutrino sample the same size as that in data set A. There were some improvements made to the detector in between the two running periods which will be discussed later in this report. We report the results from these two data sets separately, then combine them and draw our final conclusions.

THEORY

The kinematics of neutrino-nucleon elastic scattering are completely specified by two independent variables if the incident neutrino direction is known and the target nucleon is free and at rest. Since our target is liquid scintillator (CH_2), six out of eight of the target protons and six out of six of the target neutrons are inside the carbon nucleus. For these target nucleons we must also consider the effects of Fermi motion and Pauli exclusion. We discuss the corrections required later in this report. Experimentally we measured the kinetic energy T (typically $\sim$300 MeV), the rate dE/dx of energy deposition along the path, and the range R ($\sim$0.5 m) and the angle θ ($\sim$45°) of the recoiling particle. The correlation between T, dE/dx, and R identified the particle as a proton. T determines Q^2, the negative of the square of the four-momentum transfer,

$$Q^2 \equiv -(k_\nu - k_l')^2 = -(p-p')^2 = 2MT \ , \tag{1}$$

where k_ν and p are the four-momenta of the initial neutrino and nucleon, respectively, k_l' and p' are the final-state four-momenta, l refers to either ν (neutral current) or μ (charged current), M is the nucleon mass, and the muon mass is set to zero. Measurement of T along with the recoil angle with respect to the beam direction determines, in a zero-constraint fit, the incident-neutrino energy

$$E_\nu = \frac{MT}{(T^2+2MT)^{1/2}\cos\theta - T} \ . \tag{2}$$

The elastic-scattering matrix element for both neutral and charged currents takes the form[12]

$$\tau_\nu = \frac{G}{\sqrt{2}}\bar{u}(k')\gamma^\lambda(1+\gamma_5)u(k) \times \bar{u}(p')\left[\gamma_\lambda F_1(q^2) + i\frac{\sigma_{\lambda\sigma}}{2M}q^\sigma F_2(q^2) + \gamma_\lambda\gamma_5 F_A(q^2)\right]u(p) \ , \tag{3}$$

assuming a vector–axial-vector (V/A) form for the neutral current (the charged current is specifically $V-A$), assuming no second-class currents, and setting the muon mass to zero. Here $u(p)$ and $\bar{u}(p')$ are the initial and final nucleon wave functions, and $F_1(Q^2)$, $F_2(Q^2)$, and $F_A(Q^2)$ are nucleon form factors which are real dimensionless functions of Q^2. The cross section for elastic scattering is[13]

$$\frac{d\sigma}{dQ^2} = \frac{G^2M^2}{8\pi E_\nu^{\,2}}\left[A \pm B\frac{(s-u)}{M^2} + C\frac{(s-u)^2}{M^4}\right] . \tag{4}$$

Here $(+)$ refers to neutrinos and $(-)$ refers to antineutrinos,

$$s-u = 4ME_\nu - Q^2 \ , \tag{5}$$

$$A = \frac{Q^2}{M^2}\left[F_A^{\,2}\left[1+\frac{Q^2}{4M^2}\right] - F_1^{\,2}\left[1-\frac{Q^2}{4M^2}\right] + F_2^{\,2}\left[1-\frac{Q^2}{4M^2}\right]\frac{Q^2}{4M^2} + F_1F_2\frac{Q^2}{M^2}\right] , \tag{6}$$

$$B = \frac{Q^2}{M^2}F_A(F_1+F_2) \ , \tag{7}$$

$$C = \frac{1}{4}\left[F_A^{\,2} + F_1^{\,2} + F_2^{\,2}\frac{Q^2}{4M^2}\right] . \tag{8}$$

The form factors F_1, F_2, and F_A are as follows in the (very good) approximation that only couplings to the u and d quarks contribute[14]: For the charged-current interactions,

$$F_1(Q^2) = \frac{1}{(1+Q^2/4M^2)}\frac{1}{(1+Q^2/M_V^{\,2})^2}\left[\cos\theta_C\left[1+(1+\mu_p-\mu_n)\frac{Q^2}{4M^2}\right]\right] , \tag{9}$$

$$F_2(Q^2)=\frac{1}{(1+Q^2/4M^2)}\frac{1}{(1+Q^2/M_V{}^2)^2}[\cos\theta_C(\mu_p-\mu_n)]\,, \tag{10}$$

$$F_A(Q^2)=\frac{1}{(1+Q^2/M_A{}^2)^2}\cos\theta_C(1.26)\,, \tag{11}$$

where θ_C is the Cabbibo angle ($\cos\theta_C=0.974$), $M_V=0.84$ GeV, $M_A=1.00\pm0.05$ GeV, and $\mu_p=1.793$ and $\mu_n=-1.913$ are the anomalous magnetic moments of the proton and neutron, respectively. M_V, μ_p, and μ_n are measured in electron-scattering experiments and are applied here using CVC, the conserved-vector-current hypothesis. $F_A(0)$ is measured in β-decay experiments, and M_A is measured in charged-current elastic-scattering experiments.[15] For the neutral-current interactions, in the WS-GIM model, scattering from proton targets,

$$F_1(Q^2)=\frac{1}{(1+Q^2/4M^2)}\frac{1}{(1+Q^2/M_V{}^2)^2}\left[\frac{1}{2}\left[1+\frac{Q^2}{4M^2}(1+\mu_p-\mu_n)\right]-2\sin^2\theta_W\left[1+\frac{Q^2}{4M^2}(1+\mu_p)\right]\right], \tag{12}$$

$$F_2(Q^2)=\frac{1}{(1+Q^2/4M^2)}\frac{1}{(1+Q^2/M_V{}^2)^2}[\tfrac{1}{2}(\mu_p-\mu_n)-2\sin^2\theta_W\mu_p]\,, \tag{13}$$

$$F_A(Q^2)=\frac{1}{(1+Q^2/M_A{}^2)^2}\tfrac{1}{2}(1.26)\,, \tag{14}$$

where $\sin^2\theta_W$ is the single new parameter introduced in the model.

The inherent strength of the interaction is most clearly measured in the limit $Q^2\to0$, where

$$\left.\frac{d\sigma^\nu}{dQ^2}\right|_{Q^2=0}=\left.\frac{d\sigma^{\bar\nu}}{dQ^2}\right|_{Q^2=0}=\frac{G^2}{2\pi}[F_1{}^2(0)+F_A{}^2(0)]\,. \tag{15}$$

The differrential cross sections are equal at $Q^2=0$ for neutrinos and antineutrinos, and the strength of the interaction is determined independently of neutrino energy and of assumptions about the Q^2 dependence of the form factors. This limit is experimentally unattainable since $T=Q^2/2M=0$ and the recoil proton is unseen. The minimum kinetic energy necessary for the proton to be positively identified places a lower limit on the observable Q^2. The strength can be determined over a range of Q^2, $Q^2{}_{\min}<Q^2<Q^2{}_{\max}$, by measuring the ratio of the cross section for neutral-current elastic scattering to that for the charged-current quasielastic process:

$$R_\nu\equiv\left.\frac{\sigma(\nu_\mu+p\to\nu_\mu+p)}{\sigma(\nu_\mu+n\to\mu^-+p)}\right|_{Q^2{}_{\min}<Q^2<Q^2{}_{\max}}$$

and

$$R_{\bar\nu}\equiv\left.\frac{\sigma(\bar\nu_\mu+p\to\bar\nu_\mu+p)}{\sigma(\bar\nu_\mu+p\to\mu^++n)}\right|_{Q^2{}_{\min}<Q^2<Q^2{}_{\max}}. \tag{16}$$

Important information about the structure of the neutral current is derived from the comparison of neutrino and antineutrino cross sections. For a V/A interaction,

$$\frac{d\sigma^\nu}{dQ^2}-\frac{d\sigma^{\bar\nu}}{dQ^2}=\frac{G^2}{4\pi E_\nu{}^2}\frac{Q^2}{M^2}(4ME_\nu-Q^2)F_A(F_1+F_2)\,. \tag{17}$$

Equality of the two cross sections at all Q^2 would imply the absence of either vector coupling ($F_1+F_2=0$) or axial-vector coupling ($F_A=0$). The neutral-current-to-charged-current ratio of this difference has a particularly simple form:

$$\frac{(d\sigma^\nu/dQ^2-d\sigma^{\bar\nu}/dQ^2)_{\rm NC}}{(d\sigma^\nu/dQ^2-d\sigma^{\bar\nu}/dQ^2)_{\rm CC}}=\frac{\{F_A(Q^2)[F_1(Q^2)+F_2(Q^2)]\}_{\rm NC}}{\{F_A(Q^2)[F_1(Q^2)+F_2(Q^2)]\}_{\rm CC}}\,. \tag{18}$$

This expression is independent of neutrino energy. If the corresponding neutral-current and charged-current form factors have the same Q^2 dependence, as is hypothesized for the WS-GIM model, Eq. (18) is independent of Q^2, therefore independent of M_V and M_A, and equal to its value for $Q^2=0$. If the neutrino and antineutrino fluxes have the same shape as a function of energy, the four differential

cross sections can be replaced in this expression by their integrals over any given neutrino energy range and Q^2 range. In the WS-GIM model, then,

$$\frac{(\sigma_\nu-\sigma_{\bar\nu})_{\rm NC}}{(\sigma_\nu-\sigma_{\bar\nu})_{\rm CC}}\approx\frac{1}{\cos^2\theta_C}\left[\frac{1}{4}-\frac{2.793}{4.706}\sin^2\theta_W\right]. \tag{19}$$

The plots of the cross sections in Fig. 1 show why the Brookhaven neutrino beam, with $\langle E_\nu\rangle\sim 1$ GeV, was ideal for studying these reactions. At a neutrino energy of 1 GeV, the neutrino and antineutrino cross sections are distinctly different, and both are large enough to provide good rates.

In this experiment we measured the cross-section ratios R_ν and $R_{\bar\nu}$, and the differential cross sections $d\sigma^\nu/dQ^2$ and $d\sigma^{\bar\nu}/dQ^2$. With these measurements we determined $\sin^2\theta_W$ in the WS-GIM model.

DETECTOR

The experiment was performed at the BNL Alternating Gradient Synchrotron in the wide-band, horn-focused ν and $\bar\nu$ beams. The neutrino and antineutrino spectra[16] peaked near 1 GeV, ideal for neutrino-proton elastic scattering. The reactions took place in a target-detector that was massive (30 tons total, 11 tons fiducial) providing an adequate rate of the rare elastic events, and was totally sensitive (liquid scintillator) to reject background. Due to the atomic composition of the target, primarily CH_2, one quarter of the target protons were free, and the rest were bound in light carbon nuclei.

The target-detector (Fig. 2) consisted of twelve calorimeter modules[17] (each 2.7 m×2.7 m×0.4 m). Each module was optically segmented into 18 cells—16 smaller cells and 2 large cells. The 16 smaller cells (each 19 cm×23 cm×2.7 m) were viewed at each end by a 2-in. photomultiplier tube. An energy deposition $T>3$ MeV in any of the 200 independent cells triggered the recording of the precise timing and pulse height for each tube. The information from two tubes on a given cell measured the position (±15 cm) of an energy deposition along the cell and the time it occurred (±2 nsec). The total energy deposited (±15%) was calculated by summing the pulse heights in the cells that were hit, after correcting for light attenuation and scintillator nonlinearities. The large cells at the top and bottom of each module—equal in cross section to four of the smaller cells—were viewed by a 5-in. photomultiplier tube at each end and were used as a software veto against charged parti-

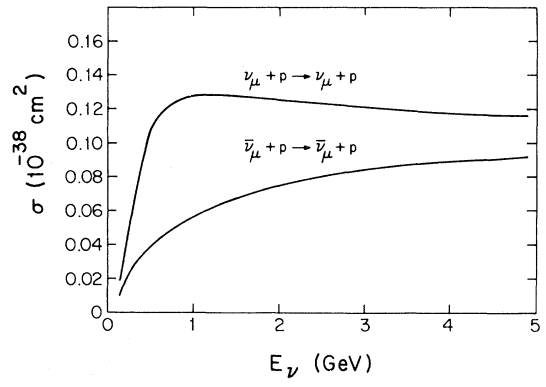

FIG. 1. Cross sections as a function of neutrino energy for $\nu_\mu+p\to\nu_\mu+p$ and $\bar\nu_\mu+p\to\bar\nu_\mu+p$ in the WS-GIM model with $\sin^2\theta_W=0.232$.

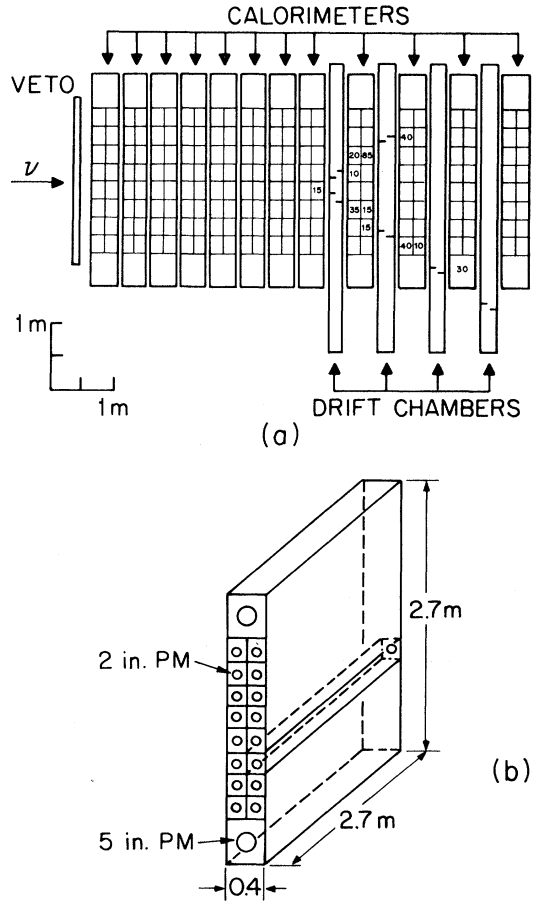

FIG. 2. (a) Side view of the apparatus showing a typical $\nu_\mu+n\to\mu^-+p$ event. The energy deposition in MeV is indicated on the cells that fired and the positions of drift-chamber hits are marked. (b) Diagram of a single calorimeter module.

cles entering from the top or bottom. A liquid-scintillator counter (2.4 m$\times$3.6 m) in front of the first calorimeter module tagged charged particles that entered from upstream.

The detector was built in two sections. In the front half of the detector the calorimeter modules were packed tightly together. This close-packed geometry had no gaps and thus was maximally sensitive to neutrons and charged particles entering from the sides, top, or bottom. In the back half of the detector four 4 m$\times$4 m drift-chamber modules were alternated with calorimeter modules. Each drift-chamber module contained two x planes and two y planes.[18] In this section of the detector we measured very well both the angle ($\pm$20 mrad) and the position ($\pm$2 mm) of any track which traversed a drift-chamber module. Behind the calorimeter, an air core magnet and two drift chambers formed a magnetic spectrometer which was used to measure the charge of small-angle muons.

The energy and time measurements by the 430 calorimeter photomultipliers and the position determinations by the 800 drift-chamber wires were continuously calibrated by horizontal beam-associated muons accepted concurrently with neutrino-induced triggers. In addition, vertical cosmic-ray muons, recorded between machine bursts, monitored the pulse height and relative timing of the phototubes. Despite the sensitive 3-MeV trigger level, the instantaneous trigger rate during the beam spill was low: only one entering charged particle triggered the device every two bursts, and an average of only 10 photomultiplier tubes fired during the 3-μsec spill time for those triggers unaccompanied by an entering charged particle.

The entire apparatus was surrounded by heavy concrete—2.4 m (10 absorption lengths) in front and 1.2 m (5 absorption lengths) on the top and sides—to shield against neutrons in the beam. This shielding coupled with the high quality of the neutrino and antineutrino beams essentially eliminated neutron-induced background. To keep potential background sources far from the detector and the beam, the detector was located 2 m from the floor and concrete ceiling and 3 m from the concrete walls.

SINGLE-PROTON-EVENT SELECTION

Figure 2 shows a stopping proton and an exiting muon characteristic of a $\nu_\mu+n\rightarrow\mu^-+p$ reaction. Events with no exiting muon, i.e., with only a single, heavily ionizing, stopping track at a large angle to the beam, were chosen as $\nu_\mu+p\rightarrow\nu_\mu+p$ candidates. The software criteria for neutral-current candidates required the following: (1) Total containment of the event: no deposition of energy above the 3-MeV threshold (a minimum-ionizing muon deposits 35 MeV in a cell) could occur in the veto counter in front of the calorimeter, in the first active 40 cm of the detector, within 40 cm of any edge of calorimeter, nor in the most downstream 20 cm of the detector. The drift chambers were used to reject events with entering or exiting charged particles. (2) A single-track topology: the track must have included ≥ 3 contiguous cells consistent with a single straight line. (3) No accompanying particles: no cell in the rest of the calorimeter could contain a deposition above the 3-MeV threshold, nor could the drift chambers indicate more than one charged particle.

The resulting single tracks could have been either protons, pions, or muons. Since $\nu_\mu+p\rightarrow\nu_\mu+n+\pi^+$ and similar reactions with a final-state pion occur at a rate comparable to that of elastic scattering, it was important to identify the source of the single-track events. The measured range, the pattern of energy depositions, and the total energy identified the stopping particle as a proton or a pion.[19] Particle type was determined from fits to the observed energy depositions by the following procedure.

Using the measured total energy of the particle, hypothetical trajectories were generated over a range of positions and angles allowed by the measured coordinates obtained from the calorimeter and drift chambers. For each trajectory the expected energy deposition in each cell was calculated and the goodness of fit for proton and pion hypotheses was evaluated by[20]

$$\chi^2=\sum_{\text{cells}}(E_{\text{meas}}-E_{\text{calc}})^2/\sigma^2\ , \tag{20}$$

where

$$\sigma/E=0.3(33\ \text{MeV}/E)^{1/2}$$

with

$$E=(E_{\text{meas}}+E_{\text{calc}})/2\ .$$

For each particle type, the trajectory was chosen which minimized χ^2. The results of such fits to a typical proton event and a typical pion event are shown in Fig. 3. Figure 4 is a scatter plot of χ_p^2 vs χ_π^2 for a sample of antineutrino data. Protons were defined by χ_p^2/(degrees of freedom) <5.0 and $\chi_p^2<\chi_\pi^2$ where the number of degrees of freedom

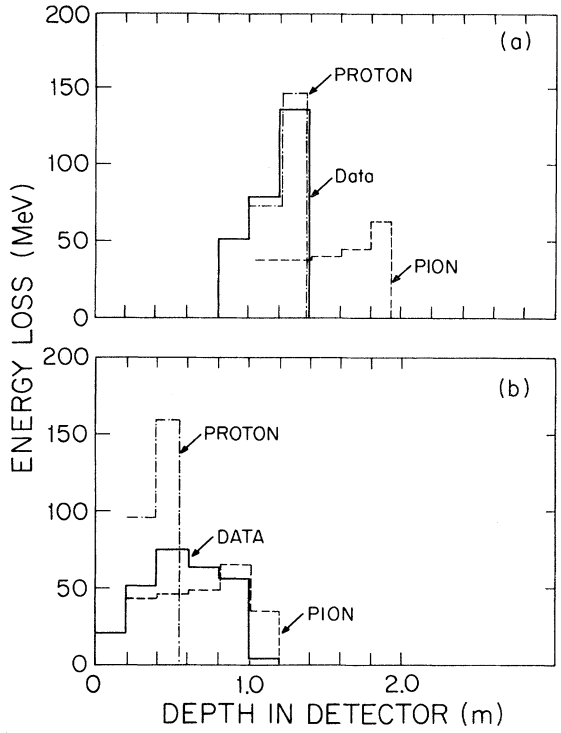

FIG. 3. Comparison of proton and pion hypotheses with observed patterns of energy deposition for (a) a proton candidate and (b) a pion candidate.

equaled the number of cells minus the one constraint (total energy). For kinetic energies below 160 MeV [$Q^2=0.30$ (GeV/c)^2], the range of the proton was on the order of the cell size and separation of protons and pions was difficult. We thus excluded all events with $T<160$ MeV from the analysis that follows. For kinetic energies greater than 160 MeV, approximately 15% of the events were ambiguous between proton and pion following this procedure, while above 210 MeV [$Q^2=0.40$ (GeV/c)^2] the ambiguity rate dropped to 10%. This ambiguity was further reduced by observation of the decay chain $\pi^+\to\mu^+ +\nu_\mu$, $\mu^+\to e^+ +\nu_e +\bar{\nu}_\mu$ discussed below. Because of the increased ambiguity and the low geometric acceptance at the lower energies (discussed below), we ultimately cut at $T>210$ MeV. In data set A we carry all events with $T>160$ MeV through the analysis to demonstrate the insensitivity of our results to this cut. In data set B we cut at $T>210$ MeV from the beginning. This procedure left us with single-proton samples of 217 neutrino events and 66 antineutrino events for $0.30<Q^2<0.90$ (GeV/c)^2 in data set A and 176 neutrino events and 149 antineutrino events for $0.40<Q^2<0.90$ (GeV/c)^2 in data set B.

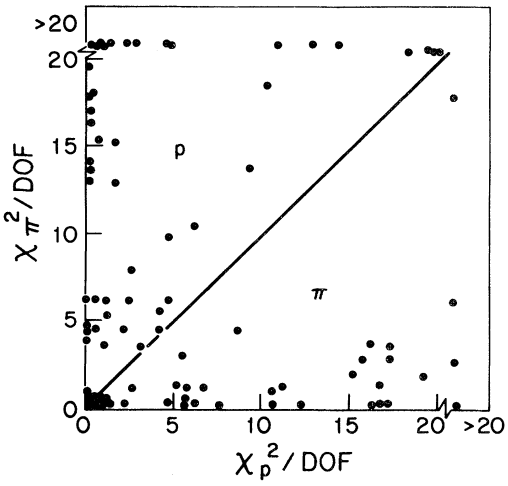

FIG. 4. Comparison of the "χ^2" per degree of freedom calculated for a proton hypothesis, χ_p^2, with that for a pion hypothesis, χ_π^2, for a sample of elastic-scattering candidates.

EVALUATION OF NEUTRON BACKGROUND

The dominant background in previous elastic-scattering experiments had been elastic neutron-proton scattering $n+p\to p+n$ with a topology identical to that of $\nu_\mu+p\to\nu_\mu+p$. Surrounding the detector with neutron absorbers does not necessarily alleviate the problem, as this passive shielding constitutes by itself a source of neutrino-induced neutrons. The solution offered by this experiment was manyfold. Added massive shielding along the beam line reduced neutron flux originating from beam losses, and neutrons reaching the experiment were attenuated by concrete shielding surrounding the detector. The detector itself was of such large size that neutrons in equilibrium with neutrinos either were absorbed in the outer regions of the device, which functioned as an active shield, or induced multiple interactions that caused such events to be excluded from the single-proton sample.

A powerful tool for identifying and eliminating neutrons produced upstream of the detector was the difference between their time of flight from the production point and the time of flight for neutrinos. The entire process of producing the neutrino beam preserved the bunched rf structure of the primary proton beam: 12 bunches, each with 30 nsec full width at half maximum, separated by 222 nsec, occurred during the 2.5-μsec extraction time. Since the neutrinos traveled with $\beta=1$, they ar-

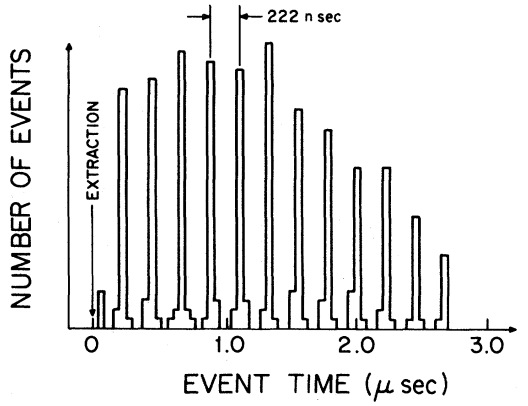

FIG. 5. Distribution of event times, relative to the beginning of the proton-beam extraction, for charged-current neutrino interactions. The distribution reflects the time structure of the primary proton beam which is preserved in the neutrino beam, and also the decreasing efficiency of extraction during the beam cycle in combination with apparatus dead time.

rived at the detector with the same timing structure. Figure 5 shows the timing distribution for a sample of charged-current events. In contrast, neutrons present in the beam were generally of low energy and traveled with $\beta << 1$. Thus neutrons originating at any substantial distance from the detector arrived later than the neutrinos from the same bunch.

In the detector, charged-current neutrino events determined the time of arrival of the neutrino bunches. Later triggers typically deposited <50 MeV and were predominantly neutron induced. Figure 6(a) shows the time distribution of a sample of neutrino-induced charged-current quasielastic events, modulo 222 nsec, which again demonstrates the narrow timing structure. The neutral-current candidates in the same figure show no single protons at a positive time after the neutrino pulse, implying that there is no neutron background in the neutrino sample. Figure 6(b) shows the same distribution for the antineutrino events. The events outside the timing window defined by the charged currents imply a neutron background within this window of $\sim(3\pm2)\%$ of the antineutrino sample.

Another neutron source arose from neutrinos interacting in the walls, floor, and ceiling of the concrete block house shielding the experiment. The dominant neutron production mechanisms were $\nu_\mu+n\rightarrow\mu^-+n+\pi^+$, and $\nu_\mu+n\rightarrow\mu^-+p$ or $\nu_\mu+p\rightarrow\mu^-+p+\pi^+$ followed by proton charge exchange in the concrete, yielding neutrons with an

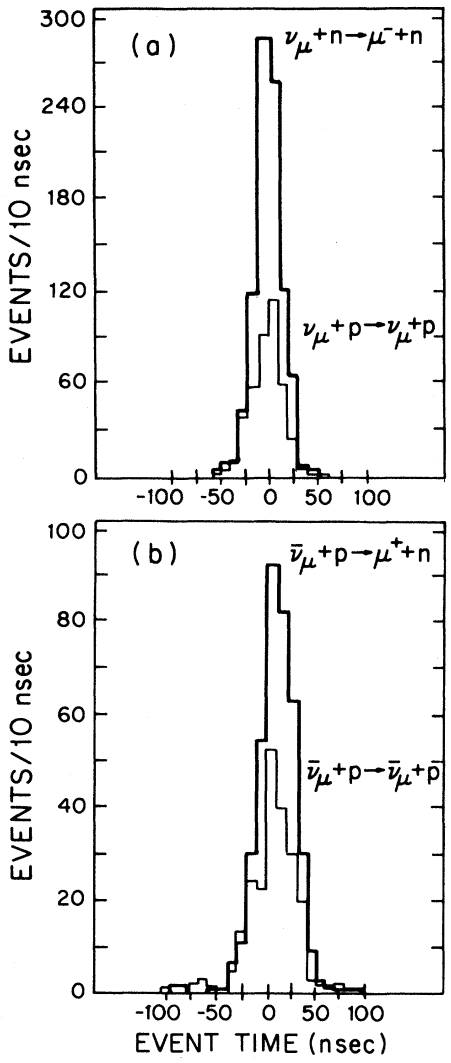

FIG. 6. Distribution of event time for (a) $\nu_\mu+p\rightarrow\nu_\mu+p$ and $\nu_\mu+n\rightarrow\mu^-+p$ events and (b) $\bar{\nu}_\mu+p\rightarrow\bar{\nu}_\mu+p$ and $\bar{\nu}_\mu+p\rightarrow\mu^+ +n$ events. Event time in this case is measured relative to the mean arrival time of the neutrinos in the "nearest" bunch. Hence, the twelve bunches shown in Fig. 5 have effectively been superimposed.

average β of 0.6. Such neutrons would reach the detector at nearly the same time as the neutrino beam. We evaluated this background by measuring the time of flight difference between neutrinos and neutrons over the length of the detector itself. Figure 7 shows, for all single-proton events, the mean event time relative to the time of the charged-current events, as a function of the distance z between the upstream shielding wall and the interaction point. Assuming that the neutrons produced

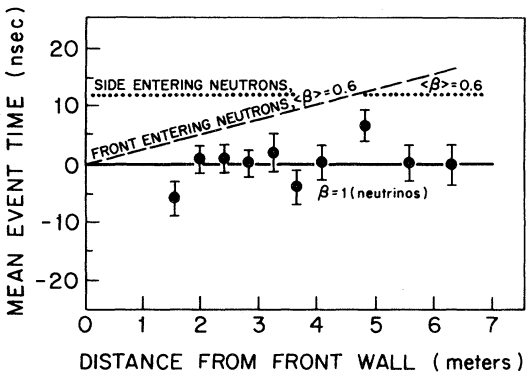

FIG. 7. Plot of the mean event time, relative to the arrival time of neutrinos at the detector, as a function of the position of the event along the length of the detector. The dashed (dotted) line indicates the expected distribution for events produced by neutrons which originate from neutrino interactions in the front (side) wall of the blockhouse.

in the front shielding wall traveled straight forward (worst case), we calculated the difference in time of flight between neutrons and neutrinos as a function of distance to the interaction point. This yielded the dashed line of Fig. 7. The data are consistent with a $\beta=1$ source, indicating that the single protons were dominantly induced by neutrinos.

Neutrons produced in the side walls would be characterized by a constant offset in the timing distribution, independent of z, equal to the neutron time of flight from the blockhouse wall to the interaction point in the calorimeter. A lower limit on this offset was obtained by assuming that all neutrons interact as soon as they penetrate the fiducial volume. A calculation of the production reactions considered above gave a mean nucleon angle of 60° for $\nu_\mu+n\rightarrow\mu^-+p$ and 35° for $\nu_\mu+n\rightarrow\mu^-+n+\pi^+$, yielding a timing offset of 12 nsec, shown by the dotted line in Fig. 7. The data were inconsistent with such an offset.

Events induced by neutrons produced in the front and side walls of the blockhouse should also have signaled their presence by attenuations away from the edges of the fiducial volume. The vertex distributions of the single-proton events both transverse to the beam [Figs. 8(a) and 8(b)] and along the beam [Figs. 8(c) and 8(d)] show no such attenuations. The vertex distribution expected from neutron-induced events [Fig. 8(e)] was calculated by generating neutrons via neutrino interactions in the shielding material, using the calculated radial

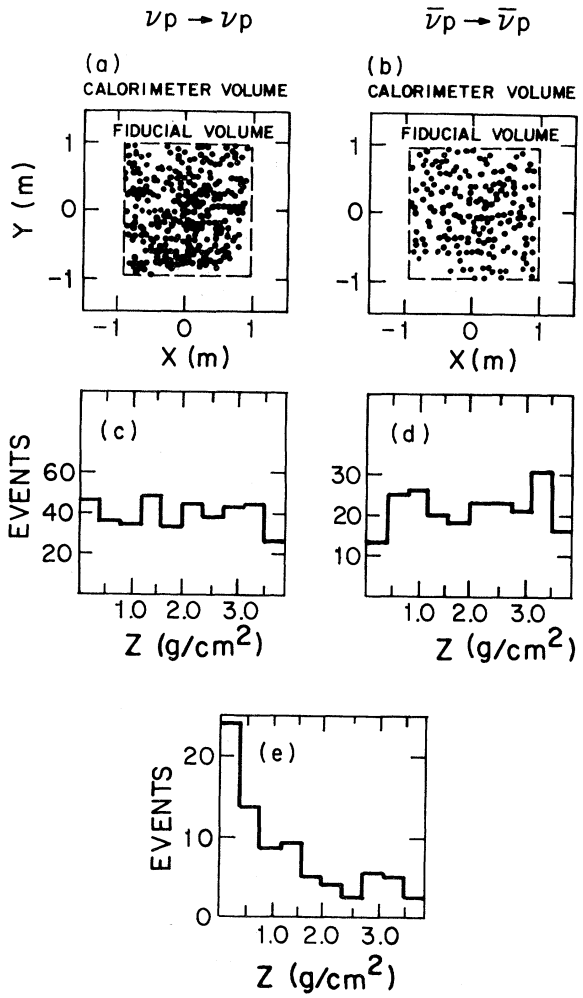

FIG. 8. Vertex distributions transverse to the beam (a) and (b), and along the beam direction (c) and (d), for single-proton candidates produced by neutrinos and antineutrinos, respectively. The histogram in (e) shows the calculated shape of the z distribution for neutrons produced by neutrino interactions in the walls of the blockhouse.

distribution of the neutrino flux.[21] These neutrons were propagated into the detector and interacted according to a standard neutron-transport code.[22] The strong attenuation expected from neutrons was absent in the data. All distributions that we have investigated are completely consistent with being neutrino-induced and are inconsistent with being neutron-induced. Quantitatively, we fit the data with a linear combination of in-time neutrons (fraction α) and neutrinos (fraction $1-\alpha$). Least-squares fits yielded upper limits of $\alpha^{\nu}<11\%$ for neutrinos and $\alpha^{\bar{\nu}}<0\%$ for antineutrinos at 98%

confidence, assuming the errors followed a Gaussian probability distribution.

Additional confirmation that the proton events arose from $\nu_\mu+p\rightarrow\nu_\mu+p$ and $\bar{\nu}_\mu+p\rightarrow\bar{\nu}_\mu+p$ was obtained from their angle–kinetic-energy correlation. Figure 9 is a scatter plot in these variables for the recoil-proton events. The relationship between T and θ was determined by the incident-neutrino energy. Kinematic curves were drawn for $E_\nu=0.5$ GeV and $E_\nu=2$ GeV; approximately 60% of the neutrino flux was expected to lie between these two energies. The data lie in the expected kinematic region. Note the distinct absence of events in the low-T, low-θ corner. In experiments using other detectors, this region has been highly populated by events induced by neutrons entering the front of the detector.

NEUTRINO-INDUCED BACKGROUND

The primary sources of background in this experiment were neutral-current single-pion production, $\nu_\mu(\bar{\nu}_\mu)+n\rightarrow\nu_\mu(\bar{\nu}_\mu)+p+\pi^-$, $\nu_\mu(\bar{\nu}_\mu)+p\rightarrow\nu_\mu(\bar{\nu}_\mu)+p+\pi^0$, $\nu_\mu(\bar{\nu}_\mu)+n\rightarrow\nu_\mu(\bar{\nu}_\mu)+n+\pi^+$, and low-energy charged currents, $\nu_\mu+n\rightarrow\mu^-+p$, $\bar{\nu}_\mu+p\rightarrow\mu^++n$ in which the π or μ was too short to be seen or was misidentified.

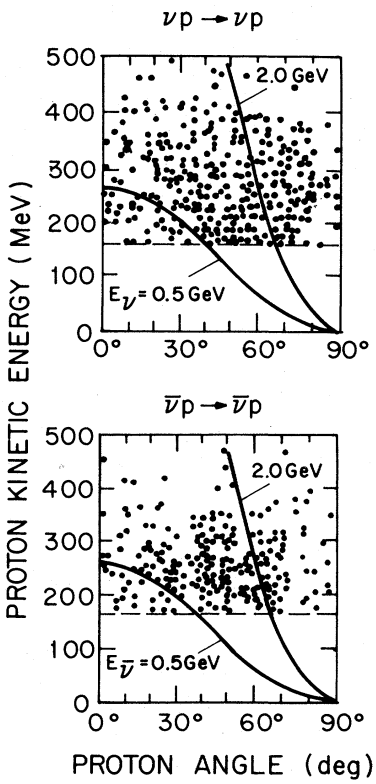

FIG. 9. Scatter plot of kinetic energy versus angle for the observed elastic-scattering candidates for ν (a) and $\bar{\nu}$ (b). The curves indicate the locus of events for $E_{\nu,\bar{\nu}}=0.5$ and 2.0 GeV.

Events containing $\mu^\pm$ or π^+ could be detected in the parts of the detector which could digitize two pulses per photomultiplier per beam spill. For data set A this capability was limited to the front half of the detector, while for data set B this capability extended over the entire detector.[23] We observed the delayed signature of the muon decay: an energetic electron (≤ 55 MeV) firing at least one cell at the end of the proton-candidate track from 0.1 to 10 μsec after the initial event. The efficiency for detecting the decay was measured using beam muons which entered and stopped within the detector. The decay detection efficiency in the front half of the detector was measured to be $(59\pm2)\%$ in the neutrino beam and $(65\pm3)\%$ in the antineutrino beam.[24] In the back half of the detector the efficiency in both beams was measured to be $(35\pm5)\%$. This lower detection efficiency was due to differences in the electronics (including higher discriminator levels in the back) and to the difference in the geometries (the decay electrons were able to escape through the drift chambers in the back without hitting a calorimeter module).

Proton candidates with a delayed pulse in a contiguous cell were considered to be muon decays and were removed from the sample. However, an unrelated later event (within the 10-μsec gate time) could mimic a decay if it were in accidental spatial coincidence with the single-proton event. The probability of this occurring was determined by selecting late events which were not contiguous with the original single prong. Assuming the late events to be distributed uniformly over the detector, the accidental rate was obtained by extrapolating the late events into the region contiguous with the single prong. The expected number of accidental "decays" was added back into the proton sample. The number of visible muon decays, combined with the accidental "decay" rates and the decay detection efficiencies, were used to extract the number of events in our data samples which contained a μ^+, μ^-, or π^+ where the muon decay was not seen. In data set A, where there was a decay detection capability over the front half of the detector only, there were 38 ± 12 missed decays in the neutrino sample and 10 ± 5 missed decays in the antineutrino sample. In data set B, where there was a decay detection capability over the entire detector, there

were 23 ± 13 missed decays in the neutrino sample and 27 ± 12 missed decays in the antineutrino sample.

Background from neutral-current production of single π^0's or π^-'s cannot be removed by this delayed timing signature. Neutral pions decay into two photons with a lifetime of 10^{-16} sec. Negative pions that come to rest are captured in atomic orbitals and absorbed by the carbon nucleus. The absorption rate is much larger than the decay rate and decay essentially never occurs. These backgrounds, however, are directly calculable.

We considered the reactions $\nu_\mu(\bar{\nu}_\mu)+p\rightarrow\nu_\mu(\bar{\nu}_\mu)+p+\pi^0$, $\nu_\mu(\bar{\nu}_\mu)+n\rightarrow\nu_\mu(\bar{\nu}_\mu)+n+\pi^0$, and $\nu_\mu(\bar{\nu}_\mu)+n\rightarrow\nu_\mu(\bar{\nu}_\mu)+p+\pi^-$ in both neutrino and antineutrino beams. (Other channels contributed negligible background.) The rates for these reactions have been measured in Gargamelle[25] in similar neutrino and antineutrino beams and in a target (90% C_3H_8 plus 10% CF_3Br) similar to that of the present experiment (CH_2 plus a small amount of structural aluminum). Nuclear effects were almost identical. The event-selection criteria were also comparable. For example, the threshold for detecting nuclear fragments in Gargamelle was 100 MeV/c ($T=5$ MeV), very close to our 3-MeV threshold. Inspection of the Gargamelle events showed that most topologies accepted in the bubble chamber[26] would also pass our cuts. Bubble-chamber events accompanied by nuclear fragments would typically be rejected by us due to the presence of extra neutrons (56% of rejected events), an extra π^0 (31% of rejected $\nu_\mu+p+\pi^-$ events), or charged nuclear fragments with more than 100 MeV of kinetic energy. The Gargamelle rates were scaled to this experiment by using the relative numbers of elastic charged-current events observed in the two experiments.[27]

The probability that $\nu_\mu(\bar{\nu}_\mu)+p\rightarrow\nu_\mu(\bar{\nu}_\mu)+p+\pi^0$ mimics $\nu_\mu(\bar{\nu}_\mu)+p\rightarrow\nu_\mu(\bar{\nu}_\mu)+p$ in our detector was calculated by superimposing actual Gargamelle[25] $\nu_\mu+p\rightarrow\nu_\mu+p+\pi^0$ events upon the calorimeter. In the calculation, vertices were distributed uniformly over the fiducial volume and the final state was rotated with a random azimuthal angle. The effect of proton interactions and saturation effects in the scintillator were taken into account, and complete electromagnetic shower propagation was employed for the protons.[28] The probability that both photons escaped detection and the remaining proton passed all requirements was $(1.6\pm0.5)\%$. The probability that $\nu_\mu(\bar{\nu}_\mu)+n\rightarrow\nu_\mu(\bar{\nu}_\mu)+n+\pi^0$ faked $\nu_\mu(\bar{\nu}_\mu)+p\rightarrow\nu_\mu(\bar{\nu}_\mu)+p$ $(0.9\pm0.4)\%$ was calculated by substituting a neutron for the proton in the Gargamelle $\nu_\mu+p+\pi^0$ events and allowing the neutron to propagate through the detector.

The process $\nu_\mu(\bar{\nu}_\mu)+n\rightarrow\nu_\mu(\bar{\nu}_\mu)+p+\pi^-$ was more difficult to treat, since when the pion is absorbed its rest mass goes both into binding energy and into the kinetic energy of nuclear fragments. The ionization energy was sometimes visible, thus vetoing the event either by destroying what would otherwise be a single-prong topology or by creating an unreasonable dE/dx pattern. Unfortunately, insufficient data exist to establish branching ratios into the final states observable in our detector. Therefore, we considered the following two limiting cases.

First we assumed that the absorption products were completely unseen, as might be the case if the absorption resulted in complete disintegration of the nucleus:

$$\pi^-+{}^{12}\mathrm{C}\rightarrow 7n+5p\ .$$

The excess (61 MeV) above the total binding energy was divided among the 12 nucleons. With an average of 5 MeV per nucleon, this reaction was unlikely to be observed because the light output of the scintillator saturates for heavily ionizing particles of this energy. Previous measurements[29] suggest that the branching ratio for this reaction is less than 1%.

In contrast, the absorption products from

$$\pi^-+{}^{12}\mathrm{C}\rightarrow n+n+{}^{10}B$$

were likely to veto $\nu_\mu(\bar{\nu}_\mu)+n\rightarrow\nu_\mu(\bar{\nu}_\mu)+p+\pi^-$ events because relatively little binding energy is lost and the two energetic neutrons ($\langle T_n\rangle\sim50$ MeV), detectable with high efficiency in the calorimeter, can destroy the single-prong topology. Final states with two fast neutrons account for approximately 10 to 40% of π^- absorption.[29]

The fraction of $\nu_\mu(\bar{\nu}_\mu)+n\rightarrow\nu_\mu(\bar{\nu}_\mu)+p+\pi^-$ events which mimic $\nu_\mu(\bar{\nu}_\mu)+p\rightarrow\nu_\mu(\bar{\nu}_\mu)+p$ is calculated for the above two cases by replacing the π^0 in the Gargamelle $\nu_\mu+p+\pi^0$ events with a π^-. If π^- absorption is unseen, an upper bound of $(5.7\pm0.8)\%$ is obtained. If π^- absorption proceeds by emitting two energetic neutrons, a lower bound of $(1.9\pm0.5)\%$ is obtained. In estimating this background, the average of the two cases was taken. The difference between the two was a measure of the systematic error in the subtraction.

The insensitivity of the calculation to the input proton and pion spectra was verified by replacing

the Gargamelle events with a sample[30] of $\nu_\mu+p \rightarrow \mu^-+p+\pi^+$ events from the BNL 7-ft bubble chamber, and suppressing the muon. The distributions of such observables as nucleon and pion energy and angles, which dominate the acceptance, were very similar in the two calculations in spite of different dynamics (charged vs neutral current) and different targets (D_2 and C_3H_8, respectively). Background levels calculated by the two methods differed by at most two standard deviations.

Finally, background from $\nu_\mu(\bar{\nu}_\mu)+n \rightarrow \nu_\mu(\bar{\nu}_\mu)+p+\pi^-$ and $\nu_\mu(\bar{\nu}_\mu)+p \rightarrow \nu_\mu(\bar{\nu}_\mu)+p+\pi^0$ due to pion absorption in the target nucleus was estimated[22] to be less than 5%, because in general the nuclear fragments were observed either directly or as excess-energy deposition at the vertex.

NUCLEAR CHARGE EXCHANGE AND $\nu_\mu+n \rightarrow \nu_\mu+n$

Events occurring in carbon were lost from our data if a reinteraction of the recoil proton inside the nucleus distorted the final state so that the event no longer passed our cuts. This loss was evaluated using a nuclear cascade code[22] which modeled the carbon nucleus as a degenerate Fermi gas with an effective nuclear radius of 4.1 fm. In the calculation, $\nu_\mu+p \rightarrow \nu_\mu+p$ protons were generated in carbon with an initial kinetic energy (before scattering in the target nucleus) of $T>210$ MeV. The results showed the following losses: (1) 8% of the final states contained a proton with $T<210$ MeV plus a neutron. (2) 5% of the final states consisted of a proton with $T>210$ MeV plus a neutron, which in turn vetoed the event approximately 50% of the time. (3) 6% of the final states consisted of two protons in which the secondary (less energetic) proton had sufficient kinetic energy to create an unreasonable dE/dx pattern, vetoing the event. The total loss of events occurring from protons bound in carbon was 16%. Since 25% of the protons in CH_2 are free, the loss in the scintillator target was approximately $(12\pm4)\%$.

Elastic neutrino-neutron scattering was expected to occur in the detector. These events appeared in our sample if the neutron exchanged charge in the target carbon nucleus, yielding a proton event indistinguishable from $\nu_\mu+p \rightarrow \nu_\mu+p$. The neutron could also scatter in the liquid, yielding a proton recoil which passed our cuts.

The probability of neutron charge exchange was studied in the same way that proton interactions with the target nucleus were treated. Of neutrons with initial kinetic energy $T_n>210$ MeV, 5% scattered to give a final-state proton with $T>210$ MeV. In most cases the original neutron also exited the nucleus, but with much diminished energy. About 50% of the time this neutron vetoed the event, yielding an effective charge-exchange probability of 2.5%.

Events in which the neutron did not charge exchange in the nucleus could be vetoed by other nuclear interactions. For instance, nuclear fragments could be left behind which vetoed the event, or the neutron energy could be reduced below the energy cut. Approximately 20% of the $\nu_\mu+n \rightarrow \nu_\mu+n$ events were vetoed in this way.

The probability that the remaining 75% of $\nu_\mu+n \rightarrow \nu_\mu+n$ events faked $\nu_\mu+p \rightarrow \nu_\mu+p$ was studied by generating $\nu_\mu+n \rightarrow \nu_\mu+n$ events throughout the whole calorimeter and propagating the neutron through the detector. The generated events were processed through the entire analysis program. The probability that a $\nu_\mu+n \rightarrow \nu_\mu+n$ event passed all cuts was 11% of the same probability for a $\nu_\mu+p \rightarrow \nu_\mu+p$ event.

The number of $\nu_\mu+n \rightarrow \nu_\mu+n$ events that appeared in our sample is a function of the cross-section ratio

$$r_\nu \equiv \frac{\sigma(\nu_\mu+n \rightarrow \nu_\mu+n)}{\sigma(\nu_\mu+p \rightarrow \nu_\mu+p)} \tag{21}$$

which depends on the isospin structure of the neutral current. Based on an analysis of deep-inelastic neutrino scattering and exclusive and inclusive neutral-current pion production, Barnett[31] estimated that $r_\nu=1.5\pm0.1$ and $r_{\bar{\nu}}=1.6\pm0.2$. After correcting for the unequal numbers of target neutrons and protons in scintillator, the fractional background of $\nu_\mu+n \rightarrow \nu_\mu+n$ events in our $\nu_\mu+p \rightarrow \nu_\mu+p$ sample was $(13\pm5)\%$.

Note that the gain in $\nu_\mu+p \rightarrow \nu_\mu+p$ candidates due to $\nu_\mu+n \rightarrow \nu_\mu+n$ events which subsequently produced a proton signature was just compensated by the loss of $\nu_\mu+p \rightarrow \nu_\mu+p$ events due to nuclear charge exchange.

The errors quoted above on the event loss due to nuclear effects $[(12\pm4)\%]$ and on the $\nu_\mu+n \rightarrow \nu_\mu+n$ background $[(13\pm5)\%]$ were determined by varying the input parameters of the models used in the calculations. The most sensitive parameter in the nuclear cascade model was the effective nuclear radius. The value used (4.1 fm) was that used in a similar model developed by the Gargamelle neutrino propane collaboration,[32] which was obtained by fitting to experimental data. Variation of this

parameter by $\pm 25\%$ caused approximately $\pm 35\%$ variation in the loss of $\nu_\mu + p \to \nu_\mu + p$ events. Alternate parametrizations of the effect of the Pauli principle, and the presence or absence of Fermi motion of the nucleons, had negligible effect on the results. For the $\nu_\mu + n \to \nu_\mu + n$ calculation, additional uncertainty arose from the neutron transport code. Variation of the neutron-carbon inelastic cross section[33] within the bounds allowed by experimental data resulted in $< \pm 20\%$ variation in the probability that $\nu_\mu + n \to \nu_\mu + n$ faked $\nu_\mu + p \to \nu_\mu + p$.

A further check on the results of this calculation was a comparison with those of the Gargamelle nuclear cascade model. Using their code[32] to calculate the same quantities yielded answers within 20% of ours.

NEUTRINOS IN THE ANTINEUTRINO BEAM

Neutrino-induced events, arising from the small neutrino content in the antineutrino beam, were a further source of background in the $\bar{\nu}$ sample. The $\nu/\bar{\nu}$ flux ratio in the $\bar{\nu}$ beam was calculated[16] to be $\approx 15\%$. The CIB collaboration has measured this ratio to be $(4.6 \pm 0.8)\%$.[10] From a small sample of $Q^2 \approx 0$ charged-current events in which the muon passed through the magnetic spectrometer behind the calorimeter, we measured[22] $\nu/\bar{\nu} < 11\%$ at 90% confidence level. This background occurred in both the $\bar{\nu}_\mu + p \to \bar{\nu}_\mu + p$ and the $\bar{\nu}_\mu + p \to \mu^+ + n$ samples, hence the corrections to numerator and denominator in the calculation of $R_{\bar{\nu}}$ tended to cancel. A net background to $\bar{\nu}_\mu + p \to \bar{\nu}_\mu + p$ of 5% was subtracted to correct for this contamination.

The CIB group also measured the $\bar{\nu}/\nu$ flux ratio in the neutrino beam and found it to be $(2.3 \pm 1.0)\%$. A net background to $\nu_\mu + p \to \nu_\mu + p$ of 2% was subtracted to correct for this contamination.

SUMMARY OF BACKGROUND CORRECTIONS

The background for both data set A and data set B are summarized in Table I. The net signal for data set A is 132 ± 21 events for $\nu_\mu + p \to \nu_\mu + p$ and 36 ± 10 events for $\bar{\nu}_\mu + p \to \bar{\nu}_\mu + p$ for $0.30 < Q^2 < 0.90$ $(\mathrm{GeV}/c)^2$. The net signal for data set B is 108 ± 19 events for $\nu_\mu + p \to \nu_\mu + p$ and 83 ± 18 events for $\bar{\nu}_\mu + p \to \bar{\nu}_\mu + p$ for $0.40 < Q^2 < 0.90$ $(\mathrm{GeV}/c)^2$.

To measure $d\sigma/dQ^2$ it is necessary to know the Q^2 dependence of the background as well as its magnitude. We found that all channels of the neutral-current single π^0 and π^- backgrounds had a similar shape that was also consistent with that expected for events with a π^+ or $\mu^\pm$ whose decay was unseen. This shape was approximately the same as that of the raw data itself for both neutrinos and antineutrinos, leading to the conclusion that each known background channel was essentially a constant fraction of the raw data. This is illustrated for the neutrino sample in Fig. 10. Consequently we did a constant-fraction background subtraction when correcting the raw data as a function of Q^2.

DETECTION EFFICIENCY

To obtain the neutral-to-charged-current cross-section ratios, R_ν and $R_{\bar{\nu}}$, we must correct the observed neutral-current rate for the acceptance under our cuts. The detection efficiency was calculated using computer generated $\nu_\mu + p \to \nu_\mu + p$ events. These were generated uniformly over the fiducial volume with random azimuthal angle and with kinetic energy and polar scattering angle appropriate to $\nu_\mu + p$ elastic scattering[34] induced by the BNL neutrino beam.[16] The response of the detector was determined and the events were subjected to the entire analysis program with requirements identical to those applied to the data. In this calculation the effect of nuclear scattering of the protons as they passed through the liquid scintillator was taken into account; it caused about a 15% event loss for $T \geq 400$ MeV, but had little effect below this energy. The acceptance was largely a geometrical effect, depending on the proton range and hence on kinetic energy as shown in Fig. 11. Low-energy events were lost because they failed to fire at least three cells, while high-energy events were lost because they left the calorimeter.

Up to this point in data set A we had included all events with $T > 160$ MeV. The acceptance, however, was very small for $T < 200$ MeV. To avoid large corrections and the possible errors they might induce, we restricted ourselves to the region of energies in which the acceptance was $> 20\%$. We thus introduced a cut requiring $0.4 < Q^2 = 2MT < 0.9$ $(\mathrm{GeV}/c)^2$ for all the data. Although we feel the data for $0.3 < Q^2 < 0.4$ $(\mathrm{GeV}/c)^2$ were less reliable due to the large acceptance correction, we also display results for data set A with those data included to show the insensitivity to this cut.

TABLE I. Subtraction of background for data sets A and B.

	Neutrinos	Antineutrinos
Data set A: $0.30<Q^2<0.90$ (GeV/c)^2		
Elastic candidates	217	66
Backgrounds		
$n+p\rightarrow n+p$	0	3±1
$\nu_\mu(\bar{\nu}_\mu)+p\rightarrow\nu_\mu(\bar{\nu}_\mu)+p+\pi^0$	18±6	6±2
$\nu_\mu(\bar{\nu}_\mu)+n\rightarrow\nu_\mu(\bar{\nu}_\mu)+n+\pi^0$	4±2	2±1
$\nu_\mu(\bar{\nu}_\mu)+n\rightarrow\nu_\mu(\bar{\nu}_\mu)+p+\pi^-$	22±7	7±2
$\nu_\mu+n\rightarrow\mu^-+p$ ($\bar{\nu}_\mu+p\rightarrow\mu^++n$) and $\nu_\mu(\bar{\nu}_\mu)+p\rightarrow\nu_\mu(\bar{\nu}_\mu)+n+\pi^+$	38±12	10±5
$\bar{\nu}$ contamination in ν	3±1	
(ν contamination in $\bar{\nu}$)		2±1
Total	85±15	30±6
Net signal	132±21	36±10
Data set B: $0.40<Q^2<0.90$ (GeV/c)^2		
Elastic candidates	176±13	149±12
Backgrounds		
$n+p\rightarrow n+p$	1±1	2±2
$\nu_\mu(\bar{\nu}_\mu)+p\rightarrow\nu_\mu(\bar{\nu}_\mu)+p+\pi^0$	17±2	13±2
$\nu_\mu(\bar{\nu}_\mu)+n\rightarrow\nu_\mu(\bar{\nu}_\mu)+n+\pi^0$	4±1	4±1
$\nu_\mu(\bar{\nu}_\mu)+n\rightarrow\nu_\mu(\bar{\nu}_\mu)+p+\pi^-$	21±2	16±2
$\nu_\mu+n\rightarrow\mu^-+p$ ($\bar{\nu}_\mu+p\rightarrow\mu^++n$) and $\nu_\mu(\bar{\nu}_\mu)+p\rightarrow\nu_\mu(\bar{\nu}_\mu)+n+\pi^+$	23±13	27±12
$\bar{\nu}$ contamination in ν	3±1	
(ν contamination in $\bar{\nu}$)		4±1
Total	68±14	66±13
Net signal	108±19	83±18

CHARGED-CURRENT NORMALIZATION

To convert the observed event rate for $\nu_\mu(\bar{\nu}_\mu)+p\rightarrow\nu_\mu(\bar{\nu}_\mu)+p$ to a cross section, we measured the effective neutrino flux by measuring the event rate of $\nu_\mu+n\rightarrow\mu^-+p$ and $\bar{\nu}_\mu+p\rightarrow\mu^++n$, processes whose cross sections are known. Two schemes for normalization were considered. The first was to measure the number of events in the same region of Q^2 as the neutral-current sample. This would give a measurement of R independent of assumptions about the exact form of the cross section. The second scheme was to measure the number of events at relatively low Q^2 and extrapolate to the Q^2 region of the neutral-current sample.

The acceptance of the magnetic spectrometer that followed the calorimeter was too small to obtain a sufficient number of events with measured muon momentum. Therefore, Q^2 had to be determined from the hadronic variables alone, as it was for the neutral-current events. For $\nu_\mu+n\rightarrow\mu^-+p$ one could simply measure the proton kinetic energy. However, this method was not directly applicable to $\bar{\nu}_\mu+p\rightarrow\mu^++n$ because a substantial fraction of the neutron energy would be lost if the neutron escaped the detector without transferring all of its energy to recoil protons. For each recoil proton, visible energy would be lost due to saturation of the liquid scintillator response. If there were many recoil protons this loss would also be significant. Due to these neutron energy losses, the large fluctuations in the losses, and the consequent distortion of the Q^2 distribution, a direct measurement of the rate of $\bar{\nu}_\mu+p\rightarrow\mu^++n$ in the $0.4<Q^2<0.9$ (GeV/c)^2 region was difficult. Therefore, we measured the flux by determining the rate at small Q^2. To minimize systematic errors in comparing neutrino and antineutrino results, the same procedure was applied to both beams.

Events were selected which contained a single muon plus additional energy deposition consistent with a proton (or neutron in the case of $\bar{\nu}_\mu+p$

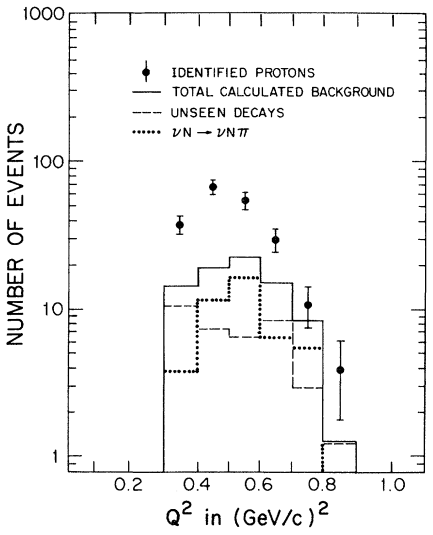

FIG. 10. Q^2 distribution for neutrino sample A of the single-proton candidates and the total calculated background which is the sum of the unseen decays indicated by the dashed line and the single-pion production indicated by the dotted line. Note that the single-proton candidates and the total calculated background have approximately the same Q^2 dependence.

$\rightarrow\mu^+ + n$). We required that the muon be a minimum ionizing track with no visible interactions, traversing at least three calorimeter modules (>2 collision lengths). The proton or neutron kinetic energy was measured as the sum of energy depositions not on the muon track plus the excess above the expected muon deposition for cells shared by both particles.

It was important to isolate the sample of charged-current quasielastic events from background events, the most significant of which arose from charged-current single-pion production. In illustrating our techniques, we will concentrate on the more difficult antineutrino analysis. Three single-pion production channels exist: $\bar{\nu}_\mu + n \rightarrow \mu^+ + n + \pi^-$, $\bar{\nu}_\mu + p \rightarrow \mu^+ + p + \pi^-$, and $\bar{\nu}_\mu + p \rightarrow \mu^+ + n + \pi^0$. The presence of a neutron in the final state of two of these reactions, and the fact that the $n + \pi^0$ final state contains only neutrals, made these events difficult to separate topologically from the desired $\mu^+ + n$ final state. However, the distributions of visible hadronic energy T_{vis} for quasielastic and single-pion events are quite different. For quasielastic events,

$$T_{\text{vis}} = \frac{Q^2}{2M} . \tag{22}$$

Since the Q^2 distribution falls rapidly with increasing Q^2, most neutrons from quasielastic events show little visible energy. For single-pion production, however,

$$T_{\text{vis}} = \frac{Q^2}{2M} + \frac{M_{N\pi}{}^2 - (M + M_\pi)^2 + M_\pi{}^2}{2M}$$

$$\approx \frac{Q^2}{2M} + 200 \text{ MeV} , \tag{23}$$

where M_π is the pion mass and $M_{N\pi}$ is the mass of the final-state $N\pi$ system. At these energies $M_{N\pi}$ is dominated[35,36] by the Δ peak at 1236 MeV/c, which we have used for the last equality. Since the Q^2 distribution[35,36] for single-pion production is similar to that for quasielastic events, we expect ~ 200 MeV more hadronic energy from the single-pion events. Events with a π^0 will have an additional 135 MeV from the pion mass.

Figure 12 compares the T_{vis} distribution of the

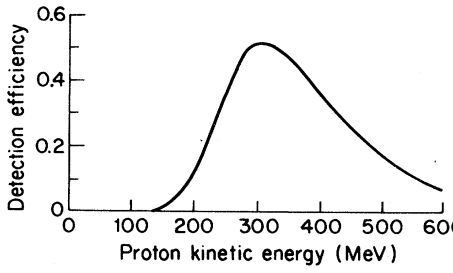

FIG. 11. Calculated detection efficiency for $\nu_\mu + p \rightarrow \nu_\mu + p$ as a function of recoil-proton kinetic energy.

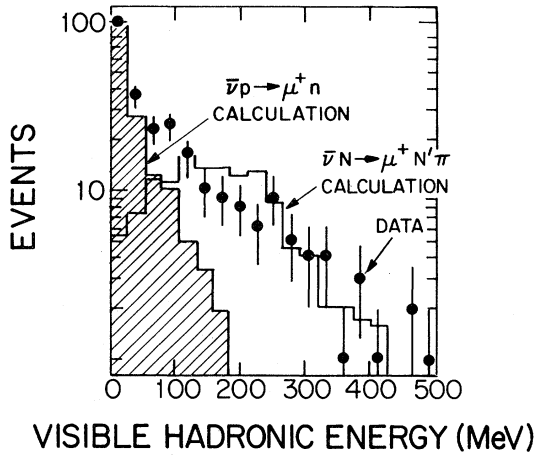

FIG. 12. Visible hadronic energy for $\bar{\nu}_\mu + p \rightarrow \mu^+ + n$ candidates with $\theta_\mu < 15°$. The shaded curve is the calculated distribution for $\bar{\nu}_\mu + p \rightarrow \mu^+ + n$, while the open curve is the $\bar{\nu}_\mu + N \rightarrow \mu^+ + N' + \pi$ distribution. The sum of the two calculations fits the data with $T_{\text{vis}} < 425$ MeV with $\chi^2 = 17.5$ for 16 degrees of freedom. Note that the ordinate is logarithmic.

data with that expected for elastic and single-pion events. The anticipated peaking for single-pion events around 200 MeV is evident. Note that an almost pure sample of $\bar{\nu}_\mu+p\to\mu^++n$ events can be isolated by requiring $T_{\rm vis}<50$ MeV. Below this cut the single-pion background is $(12\pm2)\%$. The sum of the two histograms in Fig. 12 gives a good fit ($\chi^2=17.5$ for 16 DOF) to the observed event distribution. For neutrinos, the presence of more charged particles in both the elastic and the single-pion channels shifts the $T_{\rm vis}$ distributions to higher energy. Therefore a $T_{\rm vis}<100$ MeV cut was applied to the ν data, giving a single-pion background of $(6\pm2)\%$. The errors on the single-pion background represent the errors on the single-pion production rates measured in the 12-ft bubble chamber at ANL,[35] corrected for the harder neutrino spectrum at BNL.[16]

A $T_{\rm vis}$ cut alone would have left the calculation of the acceptance for elastic events sensitive to our understanding of the behavior of the neutrons in the detector. To avoid this, we enriched our signal of small-Q^2 events by placing a requirement (whose effect was simpler to calculate) on the muon angle, θ_μ. For elastic events,

$$2MT_{\rm vis}\le Q^2=4E_\nu E_\mu\sin^2\frac{\theta_\mu}{2}\ , \tag{24}$$

where E_μ is the muon energy. Requiring θ_μ to be small ensures that $T_{\rm vis}$ is small. The θ_μ distribution peaks sharply at 10°. We therefore included only events with $\theta_\mu<15°$ in Fig. 12.

Several values for the θ_μ and $T_{\rm vis}$ cuts were tried, and the measurements of the charged-current elastic rates were independent of the choice of cuts. The fraction of $\nu_\mu+n\to\mu^-+p$ and $\bar{\nu}_\mu+p\to\mu^++n$ events accepted under these cuts was determined by analyzing simulated events superimposed on the detector. Making all corrections, we determined that there were a total of 5959 ± 409 $\nu_\mu+n\to\mu^-+p$ events and 2316 ± 167 $\bar{\nu}_\mu+p\to\mu^++n$ events for all Q^2 in data set A. We similarly determined that there were a total of 5624 ± 619 $\nu_\mu+n\to\mu^-+p$ events and 5586 ± 670 $\bar{\nu}_\mu+p\to\mu^++n$ events for all Q^2 in data set B. This extrapolation of the low-Q^2 sample to higher values of Q^2 was quite insensitive to the value of M_A chosen. Two alternate forms[13] of Pauli-principle suppression of scattering at low Q^2 were tried, a Fermi-gas calculation and a shell-model calculation, and the number of events for $0.4<Q^2<0.9$ (GeV/c)^2 varied by $\pm10\%$ (7%) for neutrinos (antineutrinos). The shell-model calculation was used.

CROSS-SECTION RATIOS

We obtained the neutral-current-to-charged-current cross-section ratios R_ν and $R_{\bar\nu}$ by dividing the acceptance corrected number of neutral-current events in the Q^2 region $0.4<Q^2<0.9$ (GeV/c)^2 by the number of charged-current events in the same Q^2 region (and when calculating R_ν also correcting for the different number of neutron and proton targets). For data set A and data set B taken separately we obtained $R_\nu=0.11\pm0.02$ and $R_{\bar\nu}=0.19\pm0.05$. Inclusion in data set A of the events with $0.3<Q^2<0.4$ (GeV/c)^2 yielded $R_\nu=0.11\pm0.02$ and $R_{\bar\nu}=0.23\pm0.06$.

Combining the results from data set A and data set B yielded

$$\begin{aligned}&R_\nu=0.11\pm0.015\ ,\\ &R_{\bar\nu}=0.19\pm0.035\ .\end{aligned}\quad 0.4<Q^2<0.9\ (\mathrm{GeV}/c)^2\ , \tag{25}$$

Using the calculated value of $R^{\rm CC}$,

$$R^{\rm CC}=\frac{\sigma(\bar{\nu}_\mu+p\to\mu^++n)}{\sigma(\nu_\mu+n\to\mu^-+p)}=0.239\quad\text{for } 0.4<Q^2<0.9\ (\mathrm{GeV}/c)^2 \tag{26}$$

we obtained

$$R^{\rm NC}=\frac{\sigma(\bar{\nu}_\mu+p\to\bar{\nu}_\mu+p)}{\sigma(\nu_\mu+p\to\nu_\mu+p)}=\frac{R_{\bar\nu}}{R_\nu}R^{\rm CC}=0.41\pm0.09\quad\text{for } 0.4<Q^2<0.9\ (\mathrm{GeV}/c)^2\ . \tag{27}$$

These results are sensitive to a number of uncertainties which we have not explicitly included up to this point. The calculation of the cross section for $\bar{\nu}_\mu+p\to\mu^++n$ as a function of Q^2 is sensitive to the shape of the antineutrino flux as a function of $E_{\bar\nu}$ for which we have no empirical evidence.[16] This is because the cross section as a function of $E_{\bar\nu}$ is not constant at the energies where the flux is significant. The neutrino cross section is nearly constant at these energies and as a result the Q^2 dependence of the energy-integrated cross section for $\nu_\mu+n\to\mu^-+p$ is relatively insensitive to the

energy dependence of the neutrino flux.

We are also sensitive to the shape of our calculated detection efficiency, particularly near $Q^2=0.4$ (GeV/c)^2 where the efficiency is small and rapidly changing. In this region of Q^2 we would be very sensitive to a small mistake in our measurement of event energies or in our evaluation of the background present.

We therefore assign a systematic error of $\sim 15\%$ to R_ν, $\sim 20\%$ to $R_{\bar\nu}$, and $\sim 25\%$ to $R^{\rm NC}$, to be added in quadrature with the errors quoted above.

DETERMINATION OF HADRONIC NEUTRAL-CURRENT COUPLINGS

We can now use our measurements of R_ν, $R_{\bar\nu}$, $d\sigma^\nu/dQ^2$, and $d\sigma^{\bar\nu}/dQ^2$ to extract information about the structure of the weak neutral current.

$R^{\rm NC}$ would be equal to unity[37] if the weak neutral current were pure vector (V), pure axial-vector (A), pure tensor (T), or any mixture of scalar (S) and pseudoscalar (P) currents. Our value of $R^{\rm NC}$ is six standard deviations from unity and rules out any of these possibilities. Further, taking the weak neutral current to be a mixture of V and A, our value of $R^{\rm NC}$ requires V *minus* A since $\sigma_{\bar\nu}<\sigma_\nu$ ($R^{\rm NC}<1$).

In the WS-GIM model there is one free parameter, $\sin^2\theta_W$. It can be determined from fits to R_ν, $R_{\bar\nu}$, $d\sigma^\nu/dQ^2$, $d\sigma^{\bar\nu}/dQ^2$, and $R^{\rm NC}$, separately or in combination. It can also be directly calculated, by solving Eq. (19) for $\sin^2\theta_W$:

$$\sin^2\theta_W=\frac{4.706}{2.793}\left[\frac{1}{4}-\cos^2\theta_C\frac{R_\nu-R_{\bar\nu}R^{\rm CC}}{1-R^{\rm CC}}\right]. \tag{28}$$

Table II shows the various values of $\sin^2\theta_W$ obtained.

The best value for $\sin^2\theta_W$ is that obtained using both $d\sigma^\nu/dQ^2$ and $d\sigma^{\bar\nu}/dQ^2$. We measure

$$\sin^2\theta_W=0.28\pm0.03\ . \tag{29}$$

All of the values for $\sin^2\theta_W$ in Table II are internally consistent and are consistent with this "best" value of $\sin^2\theta_W$. Examining Fig. 13, a plot of R_ν vs $R_{\bar\nu}$, we see that our point falls very close to the prediction of the WS-GIM model. Figure 14 is a plot of $d\sigma/dQ^2$ for both neutrinos and antineutrinos. We see that for both channels the plots are consistent with the WS-GIM model, though the slopes of our data in both channels are slightly steeper than what is predicted. In the antineutrino data, and to a lesser extent in the neutrino data, the point in the lowest-Q^2 bin [$0.4<Q^2<0.5$ (GeV/c)^2] seems to be high. This Q^2 bin had a large acceptance correction and would be particularly susceptible to background from single-pion channels. Misevaluation of either of these effects could cause the data point in this bin to be high.

Our value for $\sin^2\theta_W$ is about 1.5 standard devi-

TABLE II. Values of $\sin^2\theta_W$ obtained from the data of this experiment.

Measured quantity	$\sin^2\theta_W$
$\frac{d\sigma^\nu}{dQ^2}+\frac{d\sigma^{\bar\nu}}{dQ^2}$	0.281 ± 0.028
$\frac{d\sigma^\nu}{dQ^2}$	0.297 ± 0.034
$\frac{d\sigma^{\bar\nu}}{dQ^2}$	0.173 ± 0.099
$R_\nu+R_{\bar\nu}$	0.290 ± 0.038
R_ν	0.285 ± 0.044
$R_{\bar\nu}$	0.299 ± 0.058
$R^{\rm NC}$ (fit)	0.290 ± 0.036
$R^{\rm NC}$ [Eq. (27)]	0.281 ± 0.037

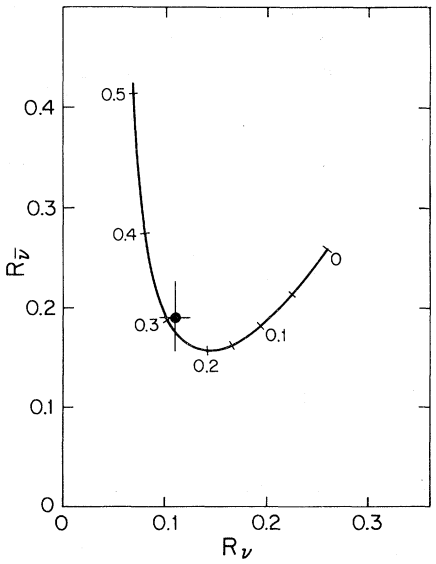

FIG. 13. Comparison of the measured values of R_ν and $R_{\bar\nu}$ with the predictions of the Weinberg-Salam model. Numbers along the curve are values of $\sin^2\theta_W$.

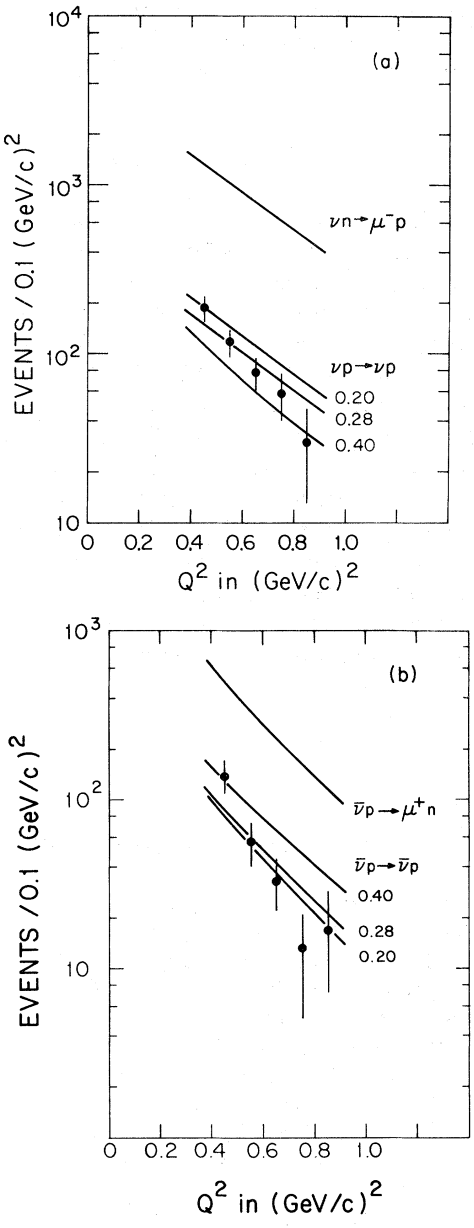

FIG. 14. Differential cross sections for (a) $\nu_\mu + p \to \nu_\mu + p$ and (b) $\bar{\nu}_\mu + p \to \bar{\nu}_\mu + p$. The solid curves are predictions for the WS-GIM model with the indicated values of $\sin^2\theta_W$.

ations higher than the world value of $\sin^2\theta_W = 0.233 \pm 0.009$. As can be seen from Table III however, our values for R_ν, $R_{\bar{\nu}}$, R^{NC}, and $\sin^2\theta_W$ are in good agreement with the results of other neutrino-proton elastic-scattering experiments done at neutrino energies near 1 GeV. The world value for $\sin^2\theta_W$ is dominated by the data from the deep-inelastic neutrino-nucleon scattering experiments and the SLAC electron-scattering asymmetry experiment. These experiments were done in very different kinematic regimes from that in which our experiment was done.

We can also analyze our data for $d\sigma^\nu/dQ^2$ and $d\sigma^{\bar{\nu}}/dQ^2$ for the three V/A form factors $F_1(0)$, $F_2(0)$, and $F_A(0)$.

Solving for all three simultaneously, we obtain two equally good solutions, both with $\chi^2 = 9.7$ for 7 degrees of freedom:

$$F_1(0) = 0.30 \pm 0.11 ,$$

$$F_2(0) = 0.67^{+0.12}_{-0.21} ,$$

$$F_A(0) = 0.56 \pm 0.03 ,$$

or

$$F_1(0) = -0.30^{+0.10}_{-0.19} ,$$

$$F_2(0) = 1.2^{+0.22}_{-0.17} ,$$

$$F_A(0) = 0.57 \pm 0.03 .$$

The errors on $F_1(0)$, $F_2(0)$, and $F_A(0)$ are large since we are solving for three variables using only ten data points. If we set $F_A(0) = 0.615$, the value predicted by the WS-GIM model independent of the value of $\sin^2\theta_W$, we find

$$F_1(0) = -0.005^{+0.11}_{-0.15} ,$$

$$F_2(0) = 0.86^{+0.12}_{-0.16} .$$

In Fig. 15 we plot the 68 and 95% confidence bounds on $F_1(0)$ and $F_2(0)$ for $F_A(0) = 0.615$, and compare with the WS-GIM model. With 95% confidence, the model is consistent with

$$0.205 < \sin^2\theta_W < 0.33 .$$

TABLE III. Summary of neutrino-proton elastic-scattering experiments.

Experiment	R_ν	$R_{\bar{\nu}}$	R^{NC}	$\sin^2\theta_W$
CIB (1981) (Ref. 10)	0.11 ± 0.03		0.44 ± 0.12	0.26 ± 0.06
Gargamelle (1978) (Ref. 8)	0.12 ± 0.06			
Aachen-Padova (1980) (Ref. 38)	0.10 ± 0.03			0.29 ± 0.21
This experiment	0.11 ± 0.015	0.19 ± 0.035	0.41 ± 0.09	0.28 ± 0.03

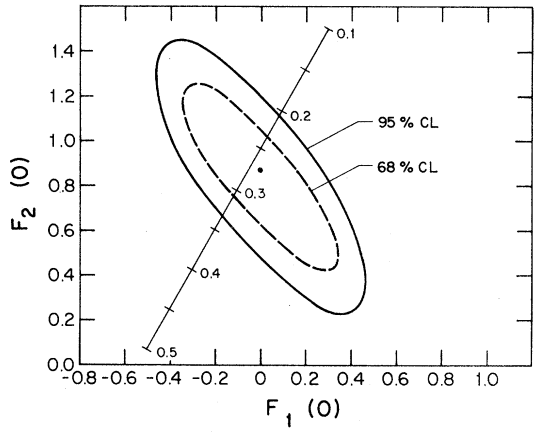

FIG. 15. $F_1(0)$ versus $F_2(0)$ for $F_A(0)=0.615$. The predictions of the Weinberg-Salam model are superimposed.

SUMMARY

We have reported new measurements of R_ν, $R_{\bar{\nu}}$, $d\sigma^\nu/dQ^2$, and $d\sigma^{\bar{\nu}}/dQ^2$ for neutrino-proton and antineutrino-proton elastic scattering. Our results are consistent with the WS-GIM model of the weak interaction and yield $\sin^2\theta_W=0.28\pm0.03$.

ACKNOWLEDGMENTS

We take this opportunity again to thank the staffs of the Brookhaven AGS, and the Harvard University and University of Pennsylvania Physics Departments for their support of this experiment. J. Blandino, M. Hearn, C. Henry, L. Holcomb, J. McElaney, R. Van Berg, and H. Weedon were responsible for the construction of the detector and its electronics. H. Foelsche, A. Pendzick, R. Rau, and W. D. Walker helped implement the experiment and expedite its running at Brookhaven. M. Bregman, M. Burka, E. Chasen, M. Claudson, M. Clements, E. Egelmen, M. Levi, M. Levine, J. Losecco, P. Rhodes, J. Yang, and M. Yudis aided in the analysis. This work was supported in part by the U. S. Department of Energy.

*Now at SUNY, Stony Brook, New York, 11794.
†Now at Laboratory for Laser Energetics, Rochester, New York, 14623.
‡Now at Cornell University, Ithaca, New York, 14853.
§Now at University of California, Irvine, California, 92717.
||Now at LBL, Berkeley, California 94720.
¶Now at University of Michigan, Ann Arbor, Michigan, 48104.

[1]S. Weinberg, Phys. Rev. Lett. 27, 1688 (1971); A. Salam, in *Elementary Particle Theory: Relativistic Groups and Analyticity (Nobel Symposium No. 8)*, edited by N. Svartholm (Almqvist and Wiksell, Stockholm, 1969), p. 367.
[2]S. L. Glashow, J. Iliopoulos, and L. Maiani, Phys. Rev. D 2, 1285 (1970).
[3]D. C. Cundy *et al.*, Phys. Lett. 31B, 478 (1970); B. Escoubes, in *La Physique du Neutrino à Haute Énergie*, proceedings of the Colloquium, École Polytechnique, Paris, 1975, edited by A. Rousset and P. Petiau (NRS, Paris, 1975), p. 265.
[4]P. Schreiner, in *Proceedings of the XVII International Conference on High Energy Physics, London, 1974*, edited by J. R. Smith (Rutherford Laboratory, Chilton, Didcot, Berkshire, England, 1974).
[5]W. Lee *et al.*, Phys. Rev. Lett. 37, 186 (1976).
[6]D. Cline *et al.*, Phys. Rev. Lett. 37, 252 (1976).
[7]H. Faissner *et al.*, in *Neutrino '77*, proceedings of the International Conference on Neutrino Physics and Neutrino Astrophysics, Baksan Valley, 1977, edited by M. A. Markov, G. V. Domogatsky, A. A. Komar, and A. N. Tavkhelidze (Nauka, Moscow, 1977), p. 164.
[8]M. Pohl *et al.*, Phys. Lett. 72B, 489 (1978).
[9]D. Cline *et al.*, Phys. Rev. Lett. 37, 648 (1976).
[10]P. Coteus *et al.*, Phys. Rev. D 24, 1420 (1981).
[11]A. Entenberg *et al.*, Phys. Rev. Lett. 42, 1198 (1979).
[12]E. Fischbach *et al.*, Phys. Rev. Lett. 37, 582 (1976); E. Fischbach *et al.*, Phys. Rev. D 15, 97 (1977).
[13]C. H. Llewellyn Smith, Phys. Rep. 3C, 262 (1972).
[14]J. E. Kim, P. Langacker, and S. Sarkar, Phys. Rev. D 18, 123 (1978); J. E. Kim, P. Langacker, M. Levine, and H. H. Williams, Rev. Mod. Phys. 53, 211 (1981).
[15]N. J. Baker *et al.*, Phys. Rev. D 23, 2499 (1981).
[16]The neutrino and antineutrino spectra have been calculated by T. Tso at Brookhaven National Laboratory using the Sanford-Wang parametrization of π and K spectra [Reports Nos. BNL 11299, JRS/CLW-1, and JRS/CLW-2 (unpublished)]. It is known, however, that the neutrino spectrum calculated by Tso overestimates the high-energy neutrino flux as determined from 7-ft bubble-chamber data (Ref. 15). In estimating backgrounds and calculating detection efficiencies we have used the measured neutrino spectral shape from the 7-ft bubble chamber. No measurement of the antineutrino spectral shape at BNL is available. Accordingly, we have used the calculated shape of the antineutrino flux with corrections to the high-energy region obtained by bringing the calculated and measured *neutrino* fluxes into agreement.

[17]A detailed description of the calorimeter appears in L. Sulak, in *Proceedings of Calorimeter Workshop, Fermilab, 1975,* edited by M. Atac (Fermilab, Batavia, Illinois, 1976), p. 155.

[18]D. C. Cheng *et al.*, Nucl. Instrum. Methods 117, 157 (1974).

[19]The ionization rate of pions and muons are sufficiently similar that we cannot distinguish them in our detector.

[20]Since the energy loss deposited in each cell is distributed according to the Landau distribution and not a normal distribution, the "χ^{2}" defined in the text will not be distributed according to a true χ^2 distribution.

[21]We have used the C. L. Wang calculation of the radial distribution of the BNL ν spectrum. On beam axis it agrees with T. Tso's calculation (Ref. 16). The calculated neutron vertex distribution is insensitive to $\pm 25\%$ variations in the ratio of ν flux in the side walls to flux on beam center.

[22]Further details may be found in J. Strait, Ph.D. thesis, Harvard University, 1978 (unpublished); W. Kozanecki, Ph.D. thesis, Harvard University, 1978 (unpublished).

[23]Further details may be found in J. Horstkotte, Ph.D. thesis, University of Pennsylvania, 1981 (unpublished).

[24]The difference between μ^- and μ^+ decay detection efficiencies is consistent with the 10% probability of μ^- capture in carbon.

[25]W. Krenz *et al.*, Nucl. Phys. B135, 45 (1978); O. Erriques *et al.*, Phys. Lett. 73B, 350 (1978). We are indebted to the Gargamelle Neutrino Propane Collaboration for providing the parameters of their reconstructed events.

[26]Small corrections are applied for the slightly different ratio of target neutrons to protons, for an $E_{\bar{\nu}} > 1$ GeV cut applied to Gargamelle $\bar{\nu}_\mu + p \rightarrow \mu^+ + n$ events but not to ours, and for charged-current events with nuclear fragments at the vertex which are rejected by the Gargamelle group but not by us.

[27]C. Longuemare (private communication).

[28]We thank R. Nelson, SLAC, for the use of the Electron-Gamma-Shower program EGS.

[29]P. Ammiraju and L. M. Lederman, Nuovo Cimento 4, 283 (1956).

[30]M. Murtagh (private communication).

[31]R. M. Barnett (private communication).

[32]M. Pohl (private communication).

[33]A. Del Guerra, Daresbury Laboratory Report No. DL/P 245, 1975 (unpublished).

[34]The Weinberg-Salam model is used to generate $\nu_\mu + p \rightarrow \nu_\mu + p$ events. The results of the calculation are insensitive to a value of the Weinberg angle.

[35]S. J. Barish *et al.*, Phys. Rev. Lett. 36, 179 (1976); J. Campbell *et al.*, *ibid.* 30, 335 (1973).

[36]E. C. M. Young, Report No. CERN 67-12, 1967 (unpublished).

[37]It has been pointed out by D. Sidhu that, since the energy spectra for neutrinos and antineutrinos are not identical, the ratio $\sigma(\bar{\nu}_\mu + p \rightarrow \bar{\nu}_\mu + p)/\sigma(\nu_\mu + p \rightarrow \nu_\mu + p)$ averaged over incident neutrino energy may deviate slightly from 1.0, even for the pure interactions.

[38]H. Faissner *et al.*, Phys. Rev. D 21, 555 (1980).